Open Access

Journal of Energy and Power Technology

LIDSEN Publishing Inc.

Research Article

Prediction of Wind Loadings on Offshore Wind Turbines Using CFD

Minghan Bao [1], Nagi Abdussamie [1,*], Faisal AlThobiani [2]

1. Centre for Maritime Engineering & Hydrodynamics, Australian Maritime College, University of Tasmania, Launceston, Australia; E-Mails: Baom@utas.edu.au; nagi.abdussamie@utas.edu.au
2. Faculty of Maritime Studies, King Abdulaziz University, Jeddah, Saudi Arabia; E-Mail: falthobiani@kau.edu.sa

* **Correspondence:** Nagi Abdussamie; E-Mail: nagi.abdussamie@utas.edu.au

Academic Editor: Andrés Elías Feijóo Lorenzo

Special Issue: Computational Fluid Dynamics and Machine Learning Methods for Offshore Renewable Energy

Journal of Energy and Power Technology
2023, volume 5, issue 1
doi:10.21926/jept.2301008

Received: December 03, 2022
Accepted: February 03, 2023
Published: February 09, 2023

Abstract

Analysing the structural response of offshore wind turbines (OWTs) requires a robust method to estimate environmental loadings associated with extreme weather conditions. This study aimed to accurately predict wind loadings on a non-rotating OWT using a Computational Fluid Dynamics (CFD) code, Ansys Fluent package. The inlet velocity boundary condition was defined as a uniform inlet wind speed and then as a Normal Wind Profile (NWP). Three large wind speeds of 25 m/s, 40 m/s and 50 m/s were tested with the aid of the RANS equations and the Shear Stress Transport (SST) turbulence model. A thorough mesh convergence study was conducted for both 2D and 3D simulations, and their results were assessed using the Richardson extrapolation method. Overall, the NWP method was found to produce larger wind forces and moments in comparison with the uniform wind speed conditions (on average 52% and 63% higher, respectively), and its predictions were consistent with the estimations obtained using the simplified drag formula recommended by offshore standards (within approx. 7% difference for wind forces). This paper provided the preliminary steps towards investigating the structural integrity of OWTs under extreme weather conditions.

Keywords
CFD; RANS; SST; extreme wind loading; offshore wind turbines; parked condition

1. Introduction

Due to its environmental-friendly nature against global warming [1], renewable energy consumption experienced a 15% annual increase rate between 2002 and 2017 [2]. However, since 2020, the energy demand has undergone a tremendous contraction due to the impact of the COVID-19 pandemic [3, 4]. For instance, compared to the 2015–2019 financial years, fossil fuel generation decreased by 28%, and nuclear energy generation decreased by 14% in 2020 [5]. Surprisingly, according to the International Energy Agency (IEA), the renewable energy sector has continuously increased even after the pandemic. The expansion of annual renewable energy capacity reached 45% (around 280 GW) in 2020, which is expected to take 90% of new power capacity expansion worldwide [6].

As a critical component of renewable energy [7], wind energy is well-known for its massive capacity [7, 8] and vast potential for various applications [2, 9]. In 2020, global wind capacity additions reached 114 GW (>90% increase). While the pace of annual market growth has slackened in 2021 and 2022, it is still 50% higher than the 2017-2019 average [6]. For many years, onshore wind technology has been the main focus of the wind energy industry due to its cost-benefit [10, 11]. Nevertheless, onshore wind turbine farms installed nearby large populated cities have recently influenced social acceptance due to their concern about noise and land limitation [12].

To help ensure electricity supply meets demand and overcome the aforementioned concerns, researchers and technology developers in the energy sector have shifted their interest to offshore wind developments [11]. According to Ren et al. [11], offshore wind turbines account for 10% of the total wind installations worldwide and are estimated to expand by over 20% by the end of 2025. The motivation towards moving wind installations further offshore can be summaried as follows. (i) offshore wind sites can be located not far from major coastal cities with less noise and visual impacts making them viable options in comparison with inland wind sites [13]. (ii) compared to onshore wind, offshore wind has higher speed and lower wind shear, contributing to higher operating efficiency [12]. (iii) offshore platforms allow for large wind turbines to be installed with higher energy output [14].

Despite the expansion trend, the offshore wind industry still faces to a number of challenges such as the high Levelized cost of electricity (LCOE), weather conditions and innovation challenges [10, 15]. It is therefore crucial to assess the optimal design/concept between bottom-mounted fixed and floating offshore wind turbines [15]. Given that the LCOE of fixed wind turbines substantially increases with the water depth, the Floating Offshore Wind Turbines (FOWTs) are perceived as a preferable design; due to their cost-efficiency for water depth over 60 m [15-17]. One important design aspect of FOWTs is the accurate prediction of the platform motions and mooring tensions associated with extreme weather conditions.

Numerical codes and simulations have recently been developed as an essential method to analyse the performance of FOWTs, as they are less limited by the scale and cost compared to model testing facilities. Many studies have adopted numerical approaches for hydrodynamic and

aerodynamic problems related to FOWTs. For instance, Y. Zhao, Yang, and He [18] developed a preliminary design of a multi-column 5-MW Tension Leg Platform Wind Turbine (TLPWT) in which the Fatigue, Aerodynamic, Structures and Turbulence (FAST) code developed by the NREL's National Wind Technology Center (NWTC) was used to predict the fully coupled motion of the TLPWT under several environmental conditions. Bae and Kim [19] developed a rotor-floater-tether coupled numerical model of the mono-column FOWT using CHARM3D, a generalised-coordinate-based Finite Element Method (FEM) program combined with FAST to solve the dynamic mooring response in time domain. Their study identified significant differences between coupled and uncoupled analysis, indicating the importance of considering coupling effects among turbines, platforms, and moorings.

Hydrodynamic solvers such as ANSYS AQWA developed on the basis of the potential flow theory do not resolve wind/current loadings such that they are typically defined by the user. Furthermore, the platform motions, power generation, and mooring tensions of an FOWT are influenced by wind loadings, in particular with large wind speeds [20]. Karimirad and Moan [21] developed a simplified method of analysing wind loadings on the 5-MW wind turbine using wind thrust coefficients generated from the horizontal axis wind turbine simulation code (HAWC2). Similar methods were also applied by Wang, Ji, Xue, and Tang [22], who neglected the wind load on the tower and the floating foundation above the still water level (SWL). More recent techniques such as Computational Fluid Dynamics (CFD) could be used to predict the wind thrust of wind turbines. Bazilevs et al. [23] developed a CFD simulation of a full-scale 5-MW wind turbine rotor under a steady uniform inlet velocity. Sezer-Uzol and Uzol [24] investigated the rotor performance under normal and extreme wind shear profiles. A more realistic wind profile was adopted by da Silva et al. [25] which takes into account the wind fluctuations by using the exponential coherence model.

While the current literature shows an increasing focus on defining accurate wind loadings on offshore wind turbines, most studies only investigated wind loading on operating wind turbines such that the scenario of the shut-down turbine "parked conditions" during extreme weather conditions remains less explored. Assessing the impact of extreme wind loadings on a non-rotating wind turbine is crucial, and closely related to the survivability and integrity of the whole structure. Additionally, limited research has considered wind loadings acting on the tower and the foundation freeboard of an OWT, which can contribute to the total wind force/moment under large wind speeds. In this paper, a non-rotating 5-MW offshore wind turbine's aerodynamic behaviour is investigated by the CFD approach through ANSYS Fluent package based on a steady incompressible Reynolds-averaged Navier–Stokes (RANS) equations with the Shear Stress Transport (SST) turbulence model. The CFD analysis aims to accurately predict wind forces and moments acting on the wind turbine of the Offshore Wind Turbine (OWT) under different wind conditions. As a validation step, a 2D simulation of airfoil cross-sections of the turbine blade is first developed by comparing the predicted lift and drag coefficients with the published results by J. Jonkman et al. [26]. The CFD model is then expanded to perform CFD analyses of the 3D wind turbine model.

The rest of the paper is structured as follows: Section 2 introduces the research methodology and the relevant theories and formulas used in the study, CFD model setup, settings, and mesh convergence studies. Section 3 presents and discusses the main CFD results of both 2D and 3D simulations. Finally, the main conclusions of our study are summarised in Section 4.

2. Materials and Methods

The overall research steps are demonstrated in the flowchart below (Figure 1), which describes how to develop 2D/3D simulations to predict wind loading on an offshore wind turbine by applying the CFD approach. The accuracy of the 3D CFD analysis of the wind turbine was first validated through a 2D simulation, while the Richardson extrapolation method was applied for both 2D and 3D mesh convergence studies. Two different inlet wind profiles (uniform and wind shear) were then investigated through CFD simulation. The results of 3D simulations were further verified through a simplified drag formula recommended by offshore standards such as the ABS MODU rules.

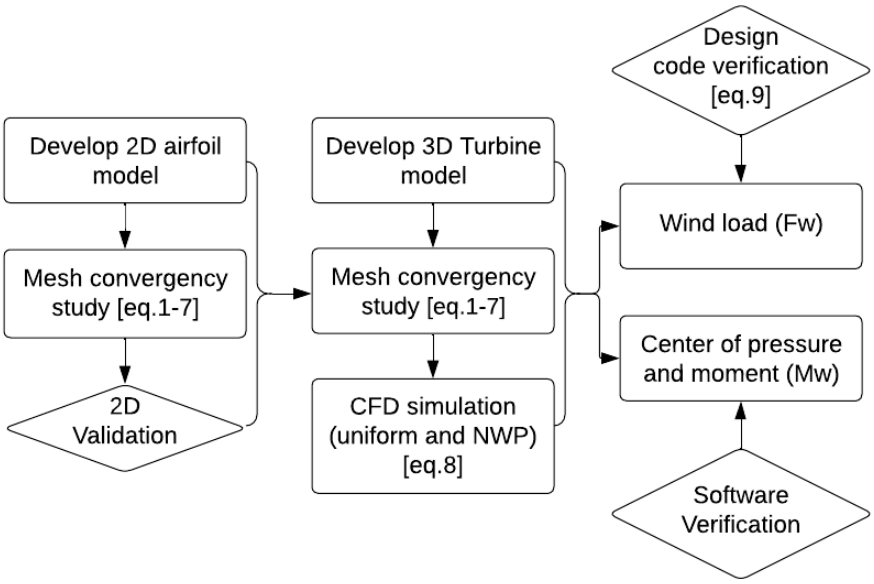

Figure 1 Research methodology flowchart.

This study treated the incompressible flow in the fluid domain as described by the RANS equations. The RANS equations divide the instantaneous velocity and pressure field terms into mean and fluctuating components. These two components are then calculated using the time-averaged method while causing additional Reynolds stresses that need to be modelled. For defining the Reynold stress, the Shear Stress Transport (SST) turbulence model implemented in the CFD code is used, as the model combines the free-stream advantages of the k-ε model with the wall-bounded advantage of the k-ω model [27].

2.1 2D Airfoil Simulations

The aerodynamic performance of the wind turbine is highly dependent on the cross-sectional foil shape [28]. The NREL 5 MW wind turbine blades are composed of 6 airfoils containing a series of DU airfoils and NACA64 foil shapes (Figure 2). Along the blade, the root portion is approximately cylindrical in shape and generally transfers to the foil shape with a certain twisting angle to enhance the aerodynamic performance [23]. In order to validate the 2D CFD simulations, three representative airfoil profiles (DU40, DU25 and NACA64) were separately selected from the blade in the vicinity of its root (DU40), middle (DU25), and tip (NACA64).

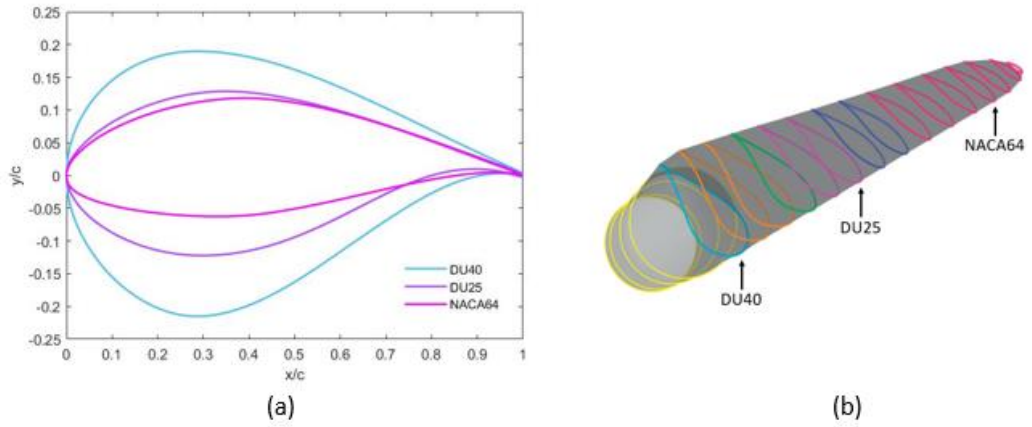

Figure 2 Airfoil cross-section of NREL 5 MW baseline wind turbine (a) and selected three representative airfoils NACA64, DU25 and DU40 (b). Adapted from [23].

According to the designed blade-pitch control system of a 5 MW baseline wind turbine [26], the wind turbine blades vary the pitching angle from 0-23.47° under different weather conditions. Thus, the airfoils are simulated within the attacking angle range -25° to 25° so that all operating conditions can be covered. Taking the NACA64 airfoil as an example, the boundary conditions and the dimensions of the numerical domain are given in Figure 3 in which the chord length of the airfoil (*L* = 1 m) has been used to establish the size of the domain (15 m × 10 m).

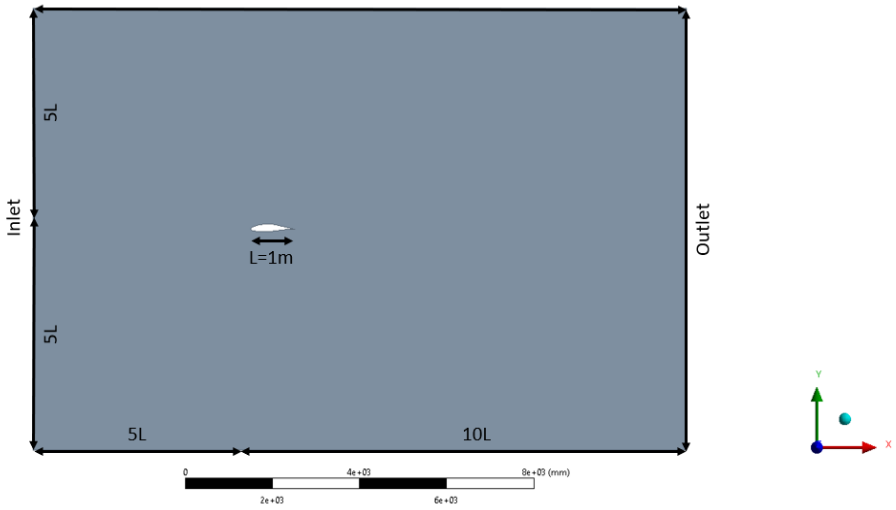

Figure 3 Computational domain of NACA 64 airfoil in ANSYS Fluent (*L* is the chord length of the airfoil = 1 m).

2.2 Mesh Convergence Study for 2D Simulations

The methodology proposed in ASME [29] are followed to apply the Richardson extrapolation in the mesh-independent study before the CFD analysis [30]. This paper selects the drag force as the standard variable to examine mesh convergence. Three different meshes with different cell counts are first generated with a certain expansion ratio r_i (the mesh refinement levels, i.e., coarse, medium, and fine, are denoted by indices 1, 2, and 3, respectively). Then the converge ratio *R* can be defined as:

$$R = \epsilon_{21}/\epsilon_{32} \tag{1}$$

$$\epsilon_{21} = \mathrm{h}_1 - \mathrm{h}_2 \tag{2}$$

$$\epsilon_{32} = \mathrm{h}_2 - \mathrm{h}_3 \tag{3}$$

where $\mathrm{h}_1, \mathrm{h}_2, \mathrm{h}_3$ are the simulation results corresponding to different mesh refinement levels 1, 2, and 3. $\epsilon_{32}, \epsilon_{21}$ are the solution differences between different mesh counts. *R* is the ratio of ϵ_{21} and ϵ_{32} which reflects the convergency pattern of simulation results. When the monotonic convergence pattern is achieved ($0 < R < 1$), the Richardson extrapolation method can be applied to define the convergence order (*p*) and extrapolation solution (C_R).

$$p = \frac{\ln(\epsilon_{32}/\epsilon_{21})}{\ln(r_i)} \tag{4}$$

$$\delta = \frac{\epsilon_{21}}{r_i^P - 1} \tag{5}$$

$$C_R = h_3 - \delta \tag{6}$$

where δ is the calculated extrapolating differences relative to the simulation result of the finest mesh refinement level. C_R is the extrapolated solution. Finally, the extrapolated relative error (ϵ_R) for each mesh size can be determined as:

$$\epsilon_R = \frac{C_i - C_R}{C_R} \tag{7}$$

The Richardson extrapolation error can be used as an indicator to reflect the accuracy of the simulation with different mesh counts. A smaller error indicates a more precise result from the CFD analysis.

As shown in Figure 4, three different levels of a surface mesh were generated for the NACA64 airfoil with increasing mesh refinement namely coarse, medium and fine mesh, respectively. To ensure a fully resolved boundary layer, 32 inflation layers with a total thickness of 42.97 mm were applied while the y+ value was equal to 1.

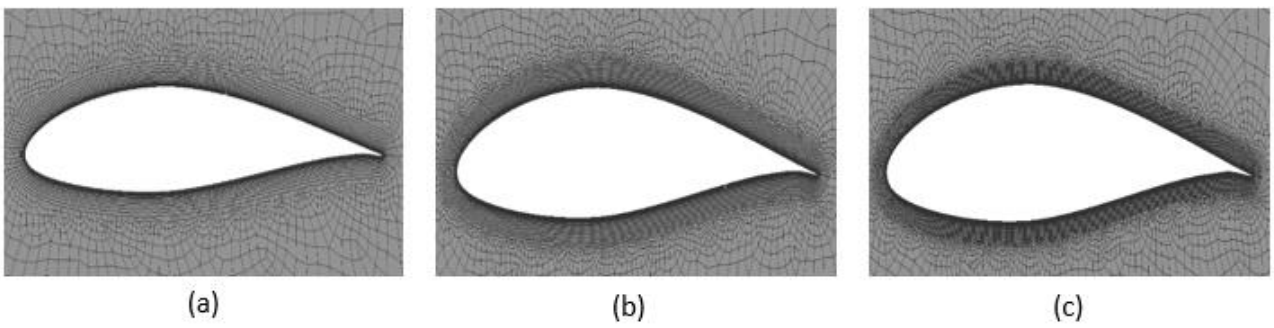

Figure 4 NACA64 airfoil mesh of three mesh refinement levels: coarse (a), medium (b) and fine (c).

The corresponding cell counts to coarse, medium and fine mesh levels are 27880, 37717 and 51185, respectively. The extrapolated relative error of each mesh refinement level was calculated and summarised in Table 1. Level three i.e. fine mesh (51185 cells and 2 hours for the computational time) provided the least relative error of 0.46%, and hence, it has been selected as the final mesh for further analyses discussed hereafter. Following the same meshing setting to the other two airfoils, the cell counts of DU25 and DU40 are 56772 and 54238, respectively. The required Reynolds number of 2×10^6 was achieved by setting the uniform inlet wind velocity at 29.5 m/s to maintain consistency with the published data of J. Jonkman et al. [26].

Table 1 Mesh convergence study results of NACA64 airfoil.

Mesh refinement level	**Cell count**	**Drag force (N)**	**Order of convergence *p* (-)**	**Extrapolated solution C_R (N)**	**Relative error (%)**	**Computational time (hours)**
Coarse	27880	87.65			7.06	0.5
Medium	37717	83.34	3.74	81.86	1.8	1
Fine	51185	82.24			0.46	2

2.3 3D OWT Simulations

In this study, the geometry of the wind turbine is a full-scale version of the experimental model used in the investigation of Murfet and Abdussamie [31] which is closely based on the NREL 5 MW baseline offshore wind turbine [26]; refer to Table 2 for the main dimensions. The wind loading is assumed acting on the structure of the OWT above the SWL, while the incoming wind direction is normal to the wind turbine rotor plane. As seen in Figure 5, the model of the floating wind turbine primarily consists of three parts, namely the rotor, the tower and the freeboard section (11.2 m high). As the focus of this investigation is on the analysis of extreme wind conditions, the control mode of the wind turbine is in shut-down position (non-rotating) with a 0° blade pitching angle "parked condition".

Table 2 Full-scale parameters of the 5 MW turbine and tower.

Parameter	**Value**
Tower height	90 m
Tower bottom diameter	6 m
Tower top diameter	3.87 m
Rotor hub diameter	3 m
Rotor diameter	126 m
Turbine blade length	61.5 m

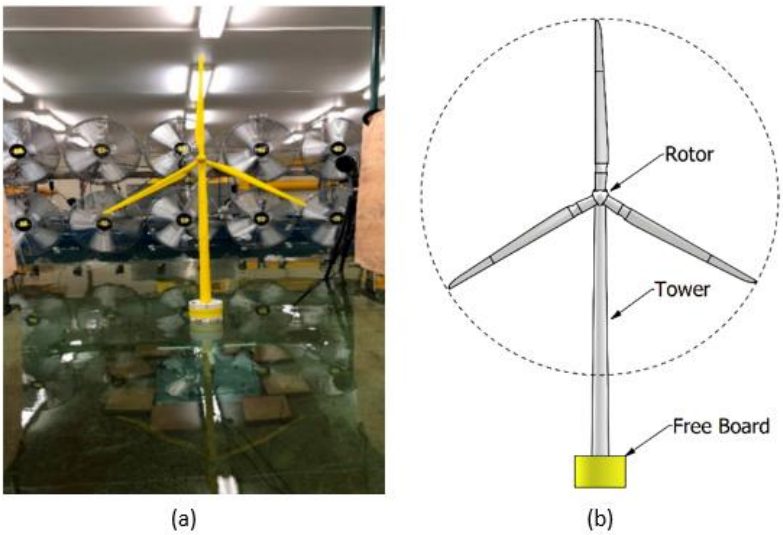

Figure 5 Experimental scaled model (a) and the equivalent full-scale 3D model (b).

The wind turbine was modelled in the Autodesk Inventor and imported into the ANSYS package for CFD simulation. To ensure the accuracy of CFD simulation, it is essential to provide a sufficient size of the computational domain. Under 50 m/s uniform wind, the wind force acting on the OWT was calculated by increasing the upstream distance off the turbine from 1*R* to 4*R* (denoted as case 1 through case 4) while the outlet boundary was kept at 6*R* downstream away from the rotor (*R* is the radius of the rotor = 63 m). As summarised in Table 3, the wind force on the OWT reduced by 66.5 kN (approx. 4%) when the inlet boundary condition location relative to the model increased from 1*R* to 2*R*. Such a difference might be caused by the unstable inlet wind velocity for not being fully-developed due to the short distance between the inlet boundary condition and the model. Beyond 2*R* distance, the wind force was found to slightly change with increasing distance.

Table 3 Verification of computational domain size of 3D wind turbine at wind speed of 50 m/s.

Case	Upstream distance off the turbine (m)	Downstream distance off the turbine (m)	Cell count	Wind force (kN)	Relative difference with case 1 (%)
1	63 (1R)	378 (6R)	4301359	1663.39	-
2	126 (2R)	378 (6R)	4328735	1596.93	-4
3	189 (3R)	378 (6R)	4349267	1597.95	-4
4	252 (4R)	378 (6R)	4367392	1596.35	-4

As a result, the final computational domain was determined as a function of the rotor radius *R* (see Figure 6) with 4*R* in width, 3*R* in height, and 8*R* in length (2*R* upstream and 6*R* downstream). In the boundary condition settings, the inlet and outlet faces were parallel to the rotor plane, which makes the air flow normally towards the turbine. The other four side faces were defined as symmetry planes such that they did not influence the air flow. Additionally, no backflow was considered during the simulation, hence, a non-reversed outlet boundary condition was applied.

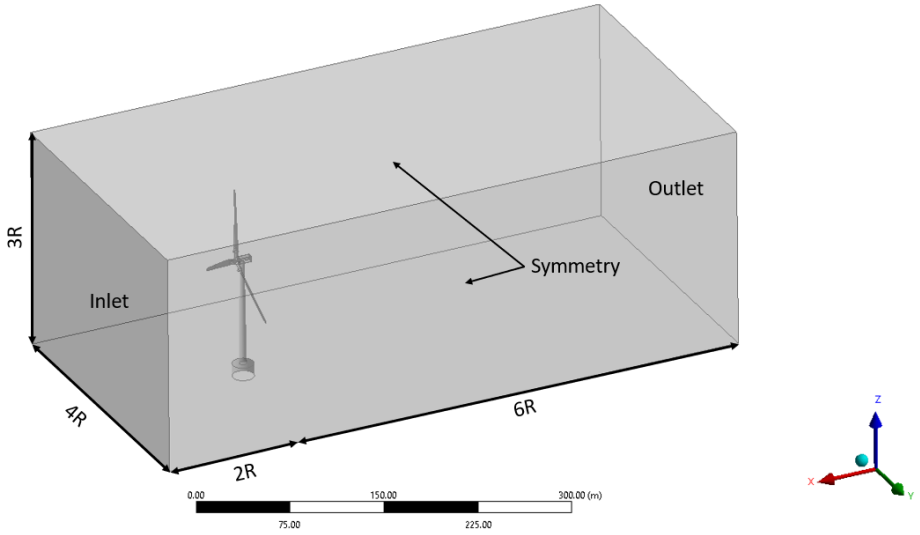

Figure 6 Computational domain of 3D wind turbine in ANSYS Fluent (R is the radius of the rotor = 63 m).

2.4 Inlet Wind Velocity for 3D Simulations

This study investigates two types of wind profiles while analysing the wind loading on the non-rotating wind turbine. The wind direction is set directly toward the wind turbine with a 0° yaw angle. The uniform free-stream wind profile is applied in the first case including three different wind speeds: the wind turbine cut-off wind speed at 25 m/s, the large offshore wind speed at 40 m/s, and the typical offshore storm wind speed at 50 m/s. With this case, a constant inlet velocity, the location of the centre of pressure on the OWT can be verified with the centre of the projected area using the Autodesk Inventor modelling software.

For the second simulation case, the normal wind profile model (NWP) is applied in which the wind speed increases with the height from the SWL. The wind speed 25 m/s, 40 m/s and 50 m/s are set as the wind speed at a reference height of 10 m above sea level where is The wind profile can be expressed by the power law [32]:

$$V_h = V_{ref}\left(\frac{z}{z_{re_f}}\right)^{\alpha} \tag{8}$$

where V_h is the average wind speed at height z above the SWL. V_{ref} is the wind speed at reference height. z_{re_f} is the reference height 10 m above the SWL. α is 0.11 for most open sea states [33].

2.5 Mesh Convergence Study for 3D Simulations

Similar to the 2D analysis, the Richardson extrapolation method was applied for the 3D wind turbine mesh converge study. The course, medium and fine structural mesh were created with a 1.25 expansion ratio of nodes number by adjusting the face size and the meshing curvature angle. During the mesh convergence study, a uniform wind speed of 50 m/s was set at the inlet boundary condition. The wind drag force was selected as the reference parameter to assess the influence of the mesh refinement level on the CFD solution. Figure 7 (a) demonstrates a monotonic converge

pattern of the wind force with increasing cell counts identified (see Table 4). The simulation's extrapolated error decreases with a higher refinement level as shown in Figure 7 (b).

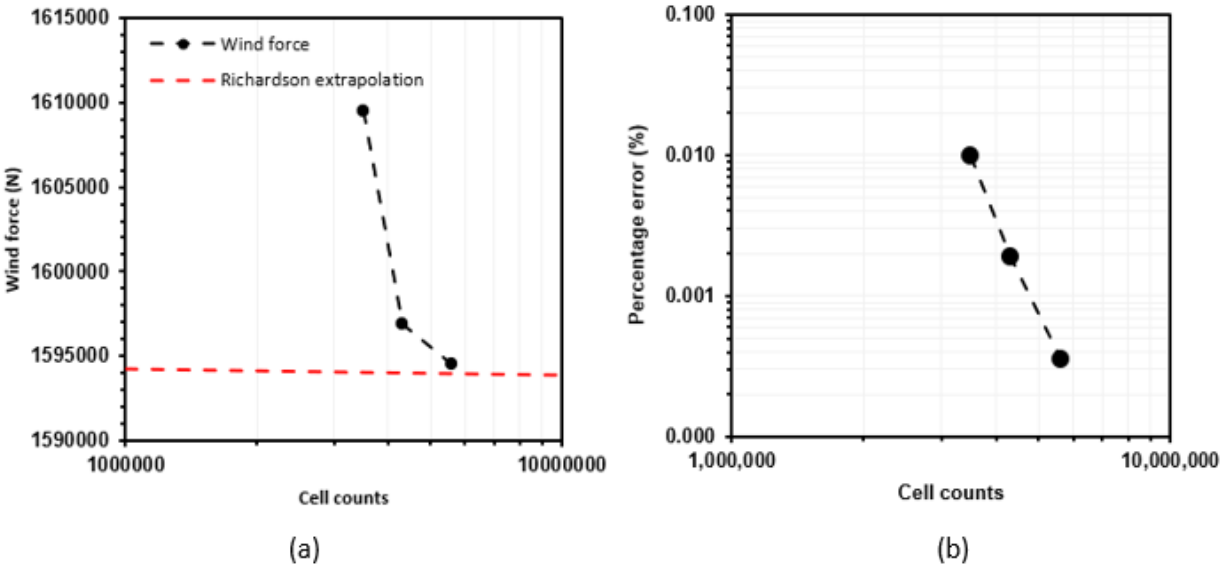

Figure 7 The simulated wind force of different mesh refinement levels (a) and extrapolated error of simulation with varying counts of mesh calculated through Richardson extrapolation method (b).

Table 4 Mesh convergence study results of 3D OWT.

Mesh refinement level	**Cell count**	**Drag force (N)**	**Order of convergence *p* (-)**	**Extrapolated solution C_R (N)**	**Relative error (%)**	**Computional time (hours)**
Coarse	3513830	1609489.46			0.98	15
Medium	4328735	1596925.32	6.28	1594197.735	0.19	26
Fine	5615110	1594473.88			0.035	72

Table 4 summarises the results of the mesh convergence study in which the order of convergence was defined as 6.28, and the extrapolated wind force was 1594.2 kN. It can be seen that the most refined mesh provided the most accurate result with only 0.035% relative error. Considering the computational time, the medium mesh size was chosen as the final mesh to save computational power while maintaining an overall accuracy with only 0.19% error.

During the final meshing, y+ = 1 was used in boundary layer meshing, resulting in 35 inflation layers with a total thickness of 128.8 mm. By applying the medium mesh refinement settings, the final mesh of the numerical domain contained 4.3 million cells. Figure 8 shows close up views of the mesh details throughout the domain and around the rotor hub and the turbine blades.

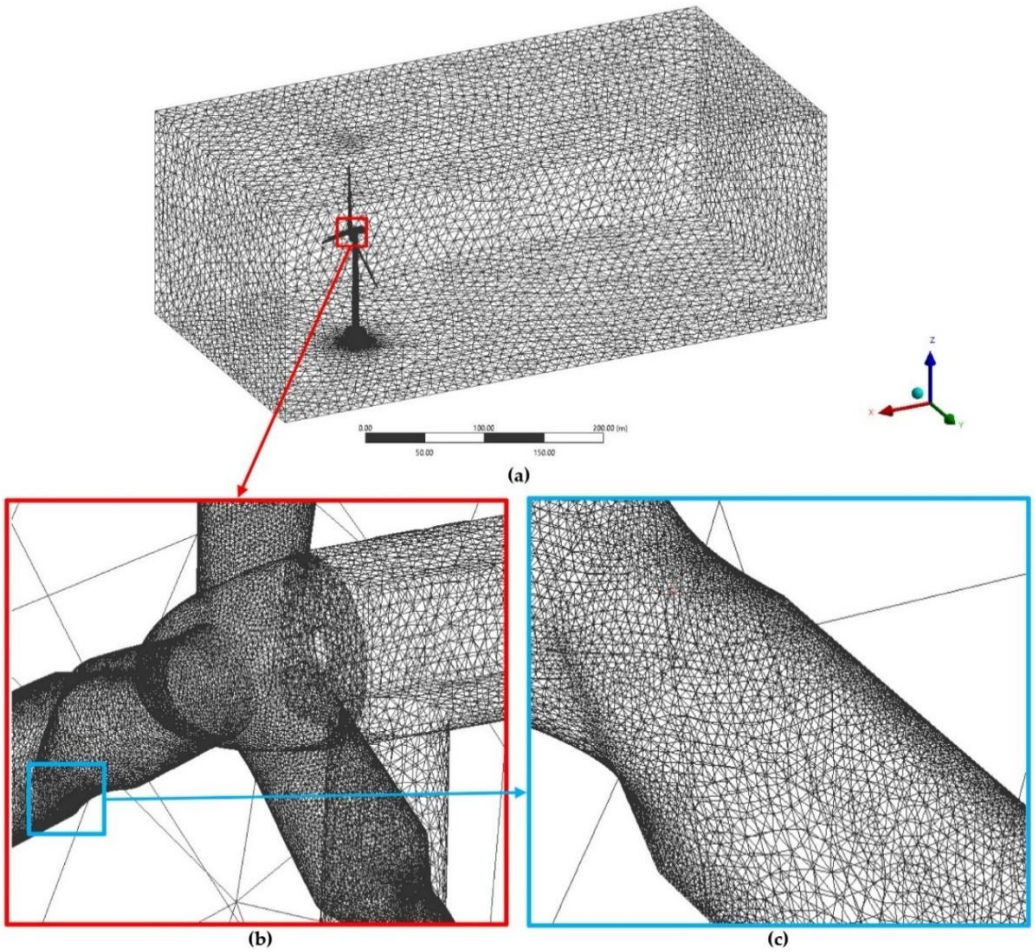

Figure 8 Final mesh of 3D OWT (a), the zoomed-in part meshing of rotor hub (b) and zoomed-in section meshing of the turbine blade (c).

2.6 3D Model Verification

For a comprehensive analysis of the wind loads acting on the offshore wind turbine, the CFD predictions were compared with the estimations obtained using a simplified drag formula based on relevant design codes for offshore structures such as API and the ABS MODU rules, where the topside of a platform is treated as 2D blocks by defining the projected area normal to the incoming wind. The wind force, F_w, acting on a 2D object located above the SWL can be estimated as [33]:

$$F_w = 0.5C_s \cdot C_h \cdot \rho \cdot V^2 \cdot A \tag{9}$$

where the ρ is the density of the air (ρ = 1.222 kg/m^3), V is the free-stream wind velocity at the reference height (Z_{ref} = 10 m). C_s is the shape coefficient of the object, C_h is the height coefficient typically given as a function of the vertical distance from the SWL to the centroid of the object, and A is the projected area of the object exposed to the wind action.

C_s and C_h can be obtained from relevant design codes such as API and the ABS MODU rules. As shown in Figure 9, the wind turbine composes of several blocks of different heights above the SWL, as denoted by the height and the assigned C_h values. The wind force acting on each block (e.g., blades, tower, freeboard) has been estimated, and then the total wind force and moment on the whole structure were obtained.

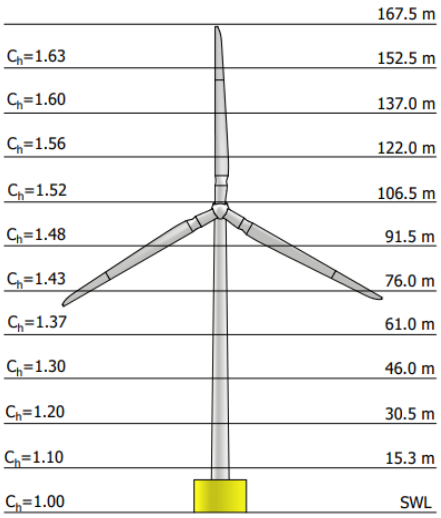

Figure 9 Height coefficients applied in wind loading estimations.

3. Results and Discussion

3.1 2D Validation Results

The CFD results of the lift and drag coefficients of DU40, DU25 and NACA64 foil shapes are compared with the published results of J. Jonkman et al. [26] in Figure 10. The CFD predictions show good agreement with the published data for the tested range of the angle of attack up to the foils reaching stall. For the post-stall condition of DU25 and NACA64 airfoil, CFD was found to overestimate the lift coefficient by about 6%, while the drag coefficient was overestimated by about 36%. The reduction in the accuracy of CFD simulations in the post-stall operation range can be explained by the fact that the RANS turbulence model cannot capture the full turbulence flow details [34].

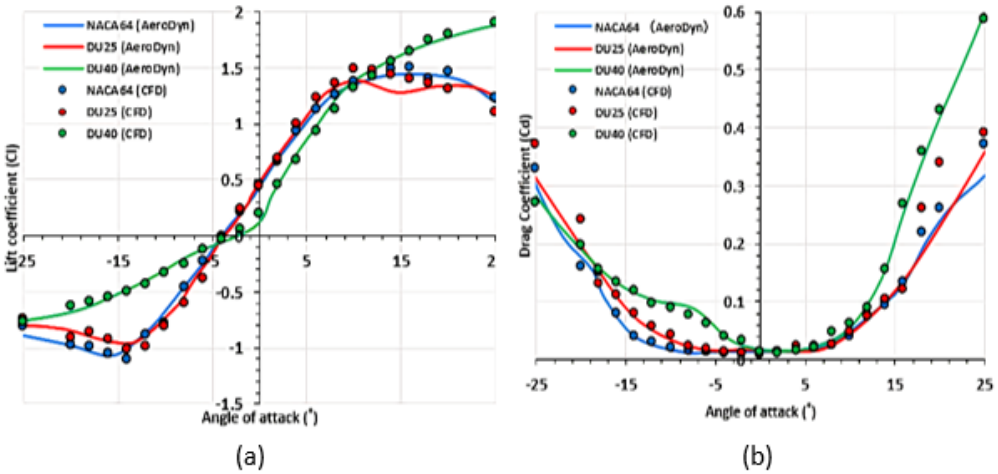

Figure 10 Comparison between CFD and AeroDyn results of 2D airfoils for lift coefficient (a) and drag coefficient (b).

Overall, the CFD model is suitable for analysing the foil sections under a low pitching angle. Since the wind turbine investigated in this study is under "shut-down" mode with 0° pitching angle, CFD predictions are acceptable.

3.2 3D OWT Results

As previously mentioned, the CFD simulation was produced by employing the steady incompressible RANS equations with the SST turbulence model. According to the different inlet wind speeds tested, the Reynolds number was estimated in the range from 5.92×10^6 to 1.18×10^7. Figure 11 shows, as an example, velocity vectors and pressure contours associated with the 50 m/s wind speed using both methods i.e. the uniform wind speed and the NWP techniques, see Figure 11 (a) and (b). Figure 11 (c) demonstrates the air pressure is evenly distributed along the OWT. Figure 11 (d) on the other hand shows a relatively low pressure at the bottom of the wind turbine and higher pressure at the turbine blade, which is consistent with the wind profile shown in Figure 11 (b) i.e. the wind velocity increases with the height.

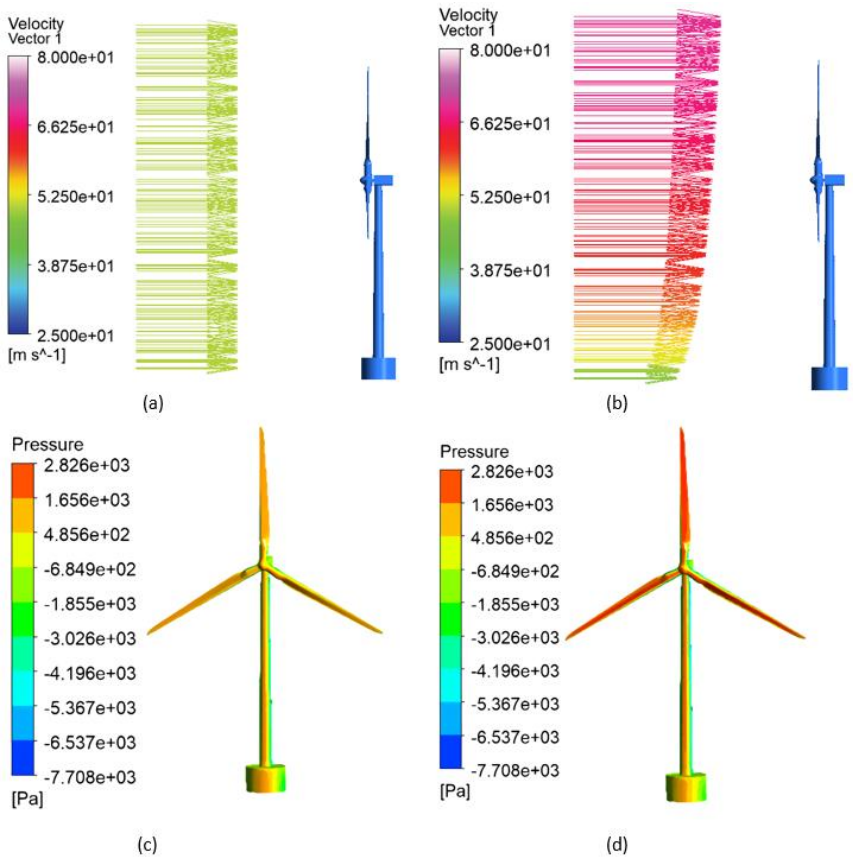

Figure 11 Air velcocity vectors and pressure contours along OWT for wind speed of 50 m/s: vecolcity vectors under uniform wind speed (a), vecolcity vectors under normal wind profile, NWP (b), pressure distribution under uniform wind speed (c) and pressure distribution under normal wind profile, NWP (d).

The CFD results of wind forces predicted using the uniform wind speed and the NWP techniques are summarised in Table 5. The wind forces acting on the OWT under a constant wind speed of 25 m/s, 40 m/s and 50 m/s are 403.98 kN, 1022.69 kN and 1596.93 kN respectively, whilst the wind

forces increases to 616.19 kN, 1562.88 kN and 2439.87 kN when the NWP technique was applied (on average a 52.7% increase). Finally, the wind forces estimated by the simplified drag formula recommended by the ABS MODU rules (Eqn. 9) were in good agreement with the CFD results for the NWP cases such that CFD predictions slightly overestimate wind forces by approximately 6.4% which can be attributed to the contribution from the frictional force component (being neglected in the simplified drag formula).

Table 5 Wind force results using different methods.

Method	**Wind speed (m/s)**	**Wind force (kN)**	**Relative difference to uniform velocity results (%)**
Uniform Wind Velocity	25	403.98	-
	40	1022.69	-
	50	1596.93	-
Normal Wind Profile (NWP)	25	616.19	52.5
	40	1562.88	52.8
	50	2439.87	52.8
ABS MODU formula (Eqn. 9)	25	568.85	40.8
	40	1456.26	42.4
	50	2327.54	45.8

The position of the wind pressure centre along the OWT was estimated by taking the average value of the CFD force results of different wind speeds. As seen in Figure 12, the pressure centre is 84.58 m above the SWL under the uniform wind speed condition, shifting to 90.54 m above the SWL (approx. 7% higher) when the NWP technique was applied. The accuracy of the CFD simulation results of the pressure centre of wind forces were further validated through the Autodesk Inventor by considering the centroid of the OWT area subjected to the wind action, and it was estimated as 83.2 m, which is quite close (as expected) to the pressure centre value obtained under the uniform wind velocity condition (with only a 1.63% difference). Table 6 summarises the results of the pressure centre and the overturning/pitching moment of the OWT about the SWL. The overturning moment was simply estimated by multiplying the wind force by the distance between the centre of pressure and the SWL.

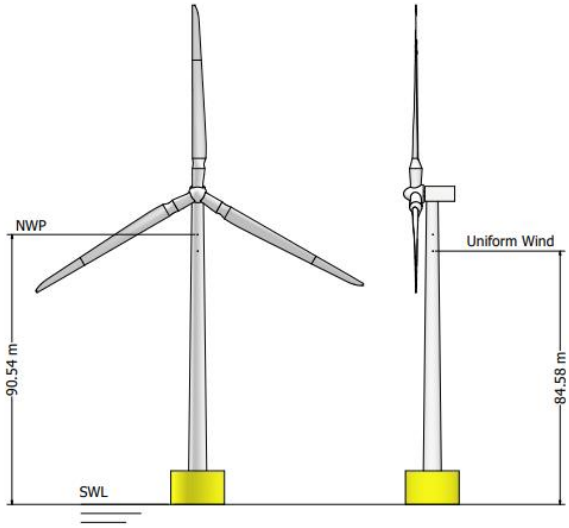

Figure 12 Location of wind pressure centre of OWT relative to the SWL under different inlet wind conditions.

Table 6 Results of wind pressure centre relative to the SWL and the resultant overturning moment.

Method	Reference wind speed (m/s)	Centre of pressure above the SWL (m)	Wind force (kN)	Overturning moment about the SWL (kN.m)
Uniform velocity	25	84.64	403.98	34192.87
	40	84.83	1022.69	86754.79
	50	84.27	1596.93	134573.29
Normal wind profile (NWP)	25	90.67	616.19	55869.95
	40	90.39	1562.88	141268.72
	50	90.55	2439.87	220930.23

4. Conclusions

This paper investigated the CFD prediction of wind loadings on a non-rotatiting OWT under extreme wind conditions through the ANSYS Fluent CFD package. The CFD analysis was based on the RANS equations with the SST turbulence model. The Richardson extrapolation method was adopted for the mesh convergency study for both 2D and 3D CFD analyses. This resulted in a final mesh of approximately 4.3M cells for the 3D wind turbine. Three extreme wind speeds of 25 m/s, 40 m/s and 50 m/s were tested, and two types of inlet wind profiles, namely a uniform inlet wind speed and a normal wind profile (NWP), were applied for the simulation at each inlet wind velocity. Wind forces and moments were the main output parameters predicted by the CFD code. Furthermore, the position of the pressure centre of OWT was also estimated by taking the average value of the CFD simulation results of different wind speeds. The main findings of this study are:

- The accuracy of the 3D CFD analysis of the wind turbine was first developed through a 2D simulation of the airfoil cross-section verified against published results, and very good agreement was achieved. This step was essential to establish an appropriate CFD modelling for the predictions of wind loadings.

- The predicted wind forces caused by the uniform wind speed of 25 m/s, 40 m/s and 50 m/s were 403.98 kN, 1022.69 kN and 1596.93 kN, respectively. On the other hand, the predicted wind forces obtained by the NWP method were 616.19 kN, 1562.88 kN and 2439.87 kN. On average, there was a 52.7% increase in wind forces when the NWP method was used. This suggested that the NWP method should be adopted during the structural analysis of OWT.
- The simplified drag formula recommended by the API/ABS produced force estimations that were consistent with the CFD predictions obtained by the NWP method (slightly large with approx. 7% difference) suggesting that the recommended drag formula can be utilized to verify CFD predictions should no experimental data of 3D OWT be available.
- For the position of the wind pressure centre of the OWT, its location was approximately 84.58 m above the SWL under the uniform wind speed condition, whilst it was estimated as 90.54 m above the SWL using the NWP method (approx. 7% higher). Such a discrepancy can be attributed to the difference in the wind profile and the corresponding force distribution along the OWT components.

The particular significance of this study lay in the accurate prediction of wind loads on the OWT under shut-down mode "parked condition" using the CFD techniques. The findings of this study can be an important milestone towards detailed analyses of the OWT's reliability and safety under extreme weather conditions. Additionally, the outcomes of this paper can be regarded as the foundation for future research to investigate the hydrodynamic and aerodynamic performance of floating OWTs under combined extreme weather conditions.

Acknowledgement

The authors would like to acknowledge the Centre for Maritime Engineering and Hydrodynamics (CMEH) of the Australian Maritime College for facilitating this study.

Author Contributions

Minghan Bao – Concepualization, CFD work, writing, editing; Nagi Abdussamie – Concepualization, supervision, advise on CFD work, writing, editing; Faisal AlThobiani – Research advisor, writing, editing.

Competing Interests

The authors have declared that no competing interests exist.

References

1. Qazi A, Hussain F, Rahim NA, Hardaker G, Alghazzawi D, Shaban K, et al. Towards sustainable energy: A systematic review of renewable energy sources, technologies, and public opinions. IEEE Access. 2019; 7: 63837-63851.
2. Sadorsky P. Wind energy for sustainable development: Driving factors and future outlook. J Clean Prod. 2021; 289: 125779.
3. Broehl J. Wind powers through pandemic [Internet]. Pelham: Wind Systems; 2021. Available from: https://www.windsystemsmag.com/wind-powers-through-pandemic/.

4. Bullard N. How wind and solar power got the best of the andemic [Internet]. Midtown Manhattan: Bloomberg Green; 2021. Available from: https://www.bloomberg.com/news/articles/2021-05-13/how-wind-and-solar-power-got-the-best-of-the-pandemic?leadSource=uverify%20wall.
5. Werth A, Gravino P, Prevedello G. Impact analysis of COVID-19 responses on energy grid dynamics in Europe. Appl Energy. 2021; 281: 116045.
6. Bahar H, Moorhouse J. Renewable energy market update: Outlook for 2021 and 2022 [Internet]. Paris: IEA; 2021. Available from: https://iea.blob.core.windows.net/assets/18a6041d-bf13-4667-a4c2-8fc008974008/RenewableEnergyMarketUpdate-Outlookfor2021and2022.pdf.
7. Dunnett S, Holland RA, Taylor G, Eigenbrod F. Predicted wind and solar energy expansion has minimal overlap with multiple conservation priorities across global regions. Proc Natl Acad Sci U S A. 2022; 119: e2104764119.
8. Marugán AP, Márquez FP, Perez JM, Ruiz-Hernández D. A survey of artificial neural network in wind energy systems. Appl Energy. 2018; 228: 1822-1836.
9. Al-Dousari A, Al-Nassar W, Al-Hemoud A, Alsaleh A, Ramadan A, Al-Dousari N, et al. Solar and wind energy: Challenges and solutions in desert regions. Energy. 2019; 176: 184-194.
10. Hevia-Koch P, Jacobsen HK. Comparing offshore and onshore wind development considering acceptance costs. Energy Policy. 2019; 125: 9-19.
11. Ren Y, Venugopal V, Shi W. Dynamic analysis of a multi-column TLP floating offshore wind turbine with tendon failure scenarios. Ocean Eng. 2022; 245: 110472.
12. Hall MT. Mooring line modelling and design optimization of floating offshore wind turbines. Victoria, BC: University of Victoria; 2013.
13. Jonkman JM. Dynamics modeling and loads analysis of an offshore floating wind turbine. Boulder, CO: University of Colorado at Boulder; 2007.
14. Musial W, Butterfield S. Future for offshore wind energy in the United States. Golden, CO: National Renewable Energy Lab.; 2004.
15. Shah KA, Meng F, Li Y, Nagamune R, Zhou Y, Ren Z, et al. A synthesis of feasible control methods for floating offshore wind turbine system dynamics. Renew Sust Energ Rev. 2021; 151: 111525.
16. Bento N, Fontes M. Emergence of floating offshore wind energy: Technology and industry. Renew Sust Energ Rev. 2019; 99: 66-82.
17. Musial WD, Beiter PC, Nunemaker J. Cost of floating offshore wind energy using new england aqua ventus concrete semisubmersible technology. Golden, CO: National Renewable Energy Lab.; 2020.
18. Zhaoy S, Yang JM, He YP. Preliminary design of a multi-column TLP foundation for a 5-MW offshore wind turbine. Energies. 2012; 5: 3874-3891.
19. Bae YH, Kim MH. Rotor-floater-tether coupled dynamics including second-order sum–frequency wave loads for a mono-column-TLP-type FOWT (floating offshore wind turbine). Ocean Eng. 2013; 61: 109-122.
20. Sebastian T, Lackner MA. Characterization of the unsteady aerodynamics of offshore floating wind turbines. Wind Energy. 2013; 16: 339-352.
21. Karimirad M, Moan T. A simplified method for coupled analysis of floating offshore wind turbines. Mar Struct. 2012; 27: 45-63.
22. Wang K, Ji C, Xue H, Tang W. Frequency domain approach for the coupled analysis of floating wind turbine system. Ships Offshore Struct. 2017; 12: 767-774.

23. Bazilevs Y, Hsu MC, Akkerman I, Wright S, Takizawa K, Henicke B, et al. 3D simulation of wind turbine rotors at full scale. Part I: Geometry modeling and aerodynamics. Int J Numer Methods Fluids. 2011; 65: 207-235.
24. Sezer-Uzol N, Uzol O. Effect of steady and transient wind shear on the wake structure and performance of a horizontal axis wind turbine rotor. Wind Energy. 2013; 16: 1-17.
25. da Silva L, de Oliveira M, Cazzolato B, Sergiienko N, Amaral G, Ding B. Statistical linearisation of a nonlinear floating offshore wind turbine under random waves and winds. Ocean Eng. 2022; 261: 112033.
26. Jonkman J, Butterfield S, Musial W, Scott G. Definition of a 5-MW reference wind turbine for offshore system development. Golden, CO: National Renewable Energy Lab.; 2009; NREL/TP-500-38060.
27. Zhao W, Cheng P, Wan D. Numerical computation of aerodynamic performances of NREL offshore 5-MW baseline wind turbine. Proceedings of the Eleventh ISOPE Pacific/Asia Offshore Mechanics Symposium; 2014 October 12-16; Shanghai, China.
28. Hartwanger D, Horvat A. 3D modelling of a wind turbine using CFD. Proceedings of the NAFEMS UK Conference 2008 “Engineering Simulation: Effective Use and Best Practice”; 2008 June 10-11; Cheltenham, United Kingdom. Leicester: The University of Leicester.
29. ASME. Procedure for estimation and reporting of uncertainty due to discretization in CFD applications. J Fluids Eng. 2008; 130: 078001.
30. Richardson LF, Gaunt JA. VIII. The deferred approach to the limit. Philos Trans Rl Soc London Ser A. 1927; 226: 299-361.
31. Murfet T, Abdussamie N. Loads and response of a tension leg platform wind turbine with non-rotating blades: An experimental study. J Mar Sci Eng. 2019; 7: 56.
32. Hsu SA, Meindl EA, Gilhousen DB. Determining the power-law wind-profile exponent under near-neutral stability conditions at sea. J Appl Meteorol Climatol. 1994; 33: 757-765.
33. ABS. Mobile offshore drilling unit part 3: Hull construction and equipment [Internet]. Houston: American Bureau of Shipping; 2018. Available from: https://daly-me.com/wp-content/uploads/2018/01/ABS-MODU-Jan-2018-Part-3.pdf.
34. Wolfe W, Ochs S, Wolfe W, Ochs S. CFD calculations of S809 aerodynamic characteristics. Proceedings of the 35th Aerospace Sciences Meeting and Exhibit; 1997 January 6-9; Reno, NV, USA. Reston: American Institute of Aeronautics and Astronautics.